Imaging bioluminescence by detecting localized haemodynamic contrast from photosensitized vasculature

Imaging bioluminescence by detecting localized haemodynamic contrast from photosensitized vasculature

Robert Ohlendorf[1,&,†], Nan Li[1,&,‡], Valerie Doan Phi Van[1], Miriam Schwalm[1], Yuting Ke[1], Miranda Dawson[1], Ying Jiang[1], Sayani Das[1], Brenna Stallings[1], Wen Ting Zheng[1] and Alan Jasanoff[1,2,3*]

[1]Department of Biological Engineering, Massachusetts Institute of Technology, 77 Massachusetts Ave., Cambridge, MA 02139
[2]Department of Brain & Cognitive Sciences, Massachusetts Institute of Technology, 77 Massachusetts Ave., Cambridge, MA 02139
[3]Department of Nuclear Science & Engineering, Massachusetts Institute of Technology, 77 Massachusetts Ave., Cambridge, MA 02139

[&]These authors contributed equally
[†]Current address: Max Planck Institute for Biological Cybernetics, Max-Planck-Ring 11, 72076 Tübingen, Germany
[‡]Current address: Advanced Imaging Research Center and Department of Neuroscience, UT Southwestern Medical Center, 2201 Inwood Rd., Dallas, TX 75390
*Corresponding author, jasanoff@mit.edu

Abstract

Bioluminescent probes are widely used to monitor biomedically relevant processes and cellular targets in living animals. However, the absorption and scattering of visible light by tissue drastically limit the depth and resolution of the detection of luminescence. Here we show that bioluminescent sources can be detected with magnetic resonance imaging by leveraging the light-mediated activation of vascular cells expressing a photosensitive bacterial enzyme that causes the conversion of bioluminescent emission into local changes in haemodynamic contrast. In the brains of rats with photosensitized vasculature, we used magnetic resonance imaging to volumetrically map bioluminescent xenografts and cell populations virally transduced to express luciferase. Detecting bioluminescence-induced haemodynamic signals from photosensitized vasculature will extend the applications of bioluminescent probes.

Editorial summary

Bioluminescent sources can be detected with magnetic resonance imaging by leveraging the light-mediated activation of vascular cells expressing a photosensitive bacterial enzyme to alter local haemodynamic contrast.

Bioluminescent reporters are widely applied in basic and preclinical biology[1, 2]. These proteins generate light by converting substrates into excited-state products that electronically relax by photon emission. By rendering luminescent enzyme activity contingent on genetic or biochemical events, a broad range of molecular and cellular processes can be studied using optical detection. Bioluminescence imaging (BLI) permits spatially resolved monitoring of luminescent reporters with high sensitivity, due to the complete absence of endogenous light sources in most organisms[3, 4]. Localization of bioluminescent probes *in vivo* is nevertheless severely compromised by scattering and attenuation of emitted light in bone and soft tissue. This is particularly a problem in the brain, where the skull impedes photon propagation, especially at short wavelengths[5]. As a result, BLI data are often limited in resolution and heavily biased toward superficial sources, and most BLI images are obtained in the form of two-dimensional projections that lack depth information. Bioluminescence tomography[6, 7] addresses this problem by using diffuse optical reconstruction methods to estimate three-dimensional light source positions in scattering tissue, but this approach usually requires *a priori* knowledge about the source distribution, as well as registration with anatomical information from an independent imaging modality.

Another way to circumvent limitations of conventional BLI would be to devise a method for converting bioluminescent output locally into a different type of signal that could be imaged in deep tissue using established noninvasive modalities like X-ray tomography, ultrasound, or magnetic resonance imaging (MRI). Although probe architectures for reversibly transducing light into MRI-detectable signals in particular have been introduced[8-13], imaging approaches using them so far lack the resolution or sensitivity to support *in vivo* BLI applications. We recently showed that engineered proteins and peptides could be used to convert molecular signals into changes in blood flow that can be sensitively detected using MRI or other hemodynamic imaging techniques. These hemodynamic imaging agents have been applied as exogenous vasoactive probes for small molecules[14] and enzymes[15, 16] or endogenously expressed "hemogenetic" reporters for intracellular calcium signalling[17]. In each case, the probes leverage the biological amplification afforded by vasodilation reflexes, the dense spatial sampling afforded by the vascular network (all tissue < 30 μm from vessels in rodent brain)[18], and the sensitivity with which vascular responses can be imaged. We reasoned that a related approach might be effective at converting photon emission from bioluminescent reporters into hemodynamic signals, thus providing a means for performing spatially resolved BLI in deep tissue and an alternative to constructing specialized reporters for noninvasive imaging modalities[19].

In this study, we implement the strategy of bioluminescence imaging using hemodynamics (BLUsH). We demonstrate that expression of a light-activated protein in vascular cells enables these cells to sense photon output from bioluminescent reporters and thereupon generate hemodynamic signals detectable in effective longitudinal relaxation time (T_2*)-weighted MRI. We apply BLUsH to detect bioluminescent cell implants and track viral expression of bioluminescent transgenes in deep brain areas of living rats. BLUsH thus provides a basis for connecting powerful optical reporter technology to state-of-the-art hemodynamic imaging in deep tissue. We anticipate that this synthesis will enable a diversity of molecular and cellular process to be studied over a range of spatiotemporal scales in living animals of any size.

Results

Characterization of BLUsH components *in vitro*. In the BLUsH paradigm, bioluminescent reporters activate light-dependent photoreceptor proteins expressed in vascular cells and stimulate downstream signalling cascades. These signalling events in turn cause local dilation of blood vessels and hemodynamic contrast detectable by MRI or other imaging modalities (**Figure 1a**). Hemodynamic changes can result from a variety of signalling pathways that ultimately inhibit or activate contraction of vascular smooth muscle cells (VSMCs)[20-22], leading to dilation or constriction of blood vessels and affecting blood flow, volume, and oxygenation. We previously engineered imaging probes that promote vasodilation via G-protein coupled receptor-mediated cyclic adenosine monophosphate (cAMP) signalling in response to target molecular cues such as enzymatic activity or signalling molecules[14-16]. For our initial implementation of BLUsH, we therefore decided to use the bacterial photoactivated adenylate cyclase (bPAC)[23] to intervene similarly, by producing intracellular cAMP in VSMCs in response to blue illumination.

To assess the feasibility of BLUsH imaging, we first characterized the light production of relevant bioluminescent enzymes. Luciferases that catalyse blue light production from coelenterazine (CTZ) substrates have been widely applied as reporters and sensors[1, 2], including for stimulation of optogenetic actuators[24]. CTZ-dependent enzymes are known for their brightness, and attenuation of their short wavelength emission in tissue is likely to promote near-field detection specificity we seek to obtain in the BLUsH approach. We compared luminescence outputs of three blue luciferases, NanoLuc[25] and engineered *Gaussia* luciferase (GLuc) variants sbGLuc and GLucM23[26]. Outputs of all luciferases are on the same order of magnitude (**Figure 1b**), but GLucM23 is 30-300% brighter than the other two; we therefore resolved to work with this protein. To get a realistic estimate of achievable light levels *in vivo*, we characterized bioluminescence of GLucM23-expressing cells at quantities and substrate doses suitable for application in

animals (250,000 cells, 95 μM CTZ). After a peak intensity of 9.9 ± 1.6 μW/cm^2 the bioluminescence output (**Figure 1c,d**) decays with a half life of 3.7 minutes (95% CI = 3.6 to 3.8 min) (**Figure 1e**). These parameters define timing and sensitivity requirements for BLUsH imaging of luciferase-expressing cells.

We next examined the ability of bPAC to activate signalling pathways in a light-dependent fashion in a CHO cell-based assay that quantitatively reports intracellular cAMP levels (**Figure 1f**). Illumination with a blue light-emitting diode (LED, 465 ± 10 nm, ~300 μW/cm^2) induced cAMP production in bPAC-expressing reporter cells, but no significant response in control cells (**Figure 1g,h**). When examined over a range of LED powers, the bPAC light response saturated with a half maximal effective dose of 26 ± 9 μW/cm^2 (**Figure 1i**); this is about twice the bioluminescent cell output, and is consistent with previous findings in bacterial fluorescence assays[27]. In order to test whether light output from bioluminescent cells is sufficient to induce equivalent responses, we exposed reporter cells expressing bPAC or control genes to luminescence from 250,000 GLucM23-expressing HEK cells incubated with 95 μM CTZ. Only bPAC-expressing cells showed substantial light-induced cAMP production (**Figure 1j**). We also demonstrated bPAC expression and blue light-sensitive activity using the bioassay of **Figure 1f** implemented in cultured VSMCs (**Figure 1k**). These results predict that bPAC should be able to promote hemodynamic responses at light doses achieved by bioluminescent reporters expressed intracellularly under biologically relevant conditions.

***In vivo* imaging of photosensitized vasculature.** Our implementation of BLUsH depends on converting endogenous blood vessels into light detectors using bPAC. To achieve bPAC expression in the cerebral vasculature of wild type rats, we used a dual adeno-associated viral (AAV) system (**Figure 2a**). The first AAV encodes green fluorescent protein (GFP)-fused Cre recombinase under control of the SM22□ promoter, which directs smooth muscle-specific expression[28, 29]. The second AAV encodes loxP-flanked bPAC, equipped with epitope and fluorescent protein tags, and placed under control of a strong constitutive promoter. Before attempting *in vivo* studies, we determined that infection with both viruses leads to bPAC expression in cultured VSMCs (**Supplementary Figure 1**). Correspondingly, coinjection into cortical and striatal brain regions in rats results in strong bPAC expression in microvascular structures (**Figure 2b,c** and **Extended Data Fig. 1**). Limitations of this approach include uneven labeling of vessels as well as some apparent off-target expression, but more homogeneous and specific brain-wide expression of bPAC could be achieved following intraventricular injection of an engineered Cre-dependent bPAC viral vector[30] into SM22□-Cre transgenic mice (**Extended Data Fig. 2**). No indication of vascular hyperactivity was seen following staining for the inflammatory marker nitrotyrosine (**Extended Data Fig. 3**). Staining for the microglial marker Iba1 likewise revealed little evidence of inflammation-associated microglial activation in bPAC-treated brain tissue (**Extended Data Fig. 4**).

To assess the ability of bPAC-expressing vessels to function as light detectors in imaging experiments, we began by examining responses to exogenous illumination in brain regions transduced with virus mixtures. MRI measurements were acquired using echo planar imaging with parameters suitable for effective detection of hemodynamic signals in rodents at high magnetic field strengths[31, 32]. Consistent with previous optogenetic studies[33], illumination with blue LED emission delivered through a fibre elicited robust signal changes in light-sensitized brain areas, but not in areas exposed to illumination in the absence of viral pretreatment (**Figure 2c** and **Extended Data Fig. 5**). Time courses of signal in regions of interest (ROIs) defined with respect to fibre positions reveal that light responses begin seconds after the LED is switched on and then decay to baseline in minutes (**Figure 2d**). Peak signals during illumination averaged 5.1 ± 0.8% in responsive and –0.1 ± 0.2% in non-responsive brains, a significant difference with Student's *t*-test $p = 0.014$ ($n = 4$) (**Figure 2e**).

The spatial distribution of MRI responses to illumination corresponds approximately to bPAC expression profiles visualized by immunohistochemistry (**Figure 2f** and **Supplementary Figure 2**). Response amplitudes fall off with distance from the fibre tip (**Figure 2g**), with a depth dependence similar to light quantification results recently reported for blue illumination in brain tissue. Neither the response rise rate (k_{on}) nor the decay rate (k_{off}) vary substantially with distance from the fibre tip, however (**Figure 2h**), indicating that response dynamics likely depend more on physiological response time courses than on photon absorption kinetics. Both hemodynamic signal change peaks and integrated response amplitudes vary monotonically with illumination intensity (**Figure 2i**), suggesting a broad, albeit nonlinear, dynamic range for vascular light sensing. Importantly, strong responses are observed with light doses as low as 0.1 mW/cm^2, comparable to levels reported in **Figure 1**, suggesting relevance of the *in vitro* results to performance of the BLUsH mechanism *in vivo*. These results thus demonstrate that vascular bPAC expression can mediate hemodynamic responses suitable for mapping illumination profiles in the rodent brain, providing a basis for BLUsH imaging of endogenous luminescent probes.

BLUsH imaging of luminescent xenografts. A common application of conventional BLI is the tracking of luminescent reporter-expressing cells *in vivo*, but accomplishing this in the brain is particularly challenging.

To assess the ability of BLUsH to detect luciferase expression *in vivo*, we therefore examined whether the method could enable luminescent cell visualization in deep brain tissue. We established BLUsH detection regions in the striatum of healthy rats by injecting AAVs encoding vessel-targeted bPAC. Control regions expressing a fluorescent marker in place of bPAC were established in contralateral hemispheres. After six weeks to permit BLUsH vascular light sensitivity to develop, xenografts of 500,000 cells expressing GLucM23 luciferase equivalent to those used in the experiments of **Figure 1,** were implanted into the photosensitized and control brain regions (**Figure 3a**).

To perform BLUsH imaging of the xenografts, continuous MRI scanning was performed before, during, and after CTZ substrate infusion via intracranial cannulae implanted over the bioluminescent cells. This procedure induced large hemodynamic signals in the area of the xenografts implanted in photosensitized brain hemispheres, but not in control non-bPAC virus-treated or untreated regions (**Figure 3b**). Mean maps of the positive BLUsH responses averaged over experiments reveal a compact spatial profile with minimal standard deviation over animals (**Figure 3c**), whereas control data from luminescent cells in untreated tissue remain within error of baseline (**Supplementary Figure 3**). BLUsH signal arising from the luminescent cells displays an average full width at half-maximum (FWHM) of 1.3 ± 0.2 mm ($n = 5$), similar to the signal width predicted for an implant with 1 mm diameter (**Figure 3d**). This is also consistent with visualization of representative implants by postmortem histology (**Figure 3e**), illustrating the approximate spatial correspondence of BLUsH signal changes with location of luminescence cells in light-sensitized brain tissue. Conventional BLI with a high-sensitivity camera was also able to visualize equivalent luciferase-expressing cell implants *in vivo* (**Extended Data Fig. 6**), but with a FWHM of 2.6 ± 0.3 mm that was more than twice the xenograft diameter and significantly greater than the BLUsH FWHM (*t*-test $p = 0.01$, $n = 4, 5$). Xenografts expressing GLucM23 and the red-shifted luciferase Akaluc[34] (both $n = 2$) displayed similar FWHM in this analysis.

The time course of BLUsH MRI responses in the cell implant experiments shows a rise within seconds of CTZ infusion that is not observed in control non-BLUsH conditions (**Figure 3f**). Analysis of the effective dose of CTZ delivery versus signal change indicates a monotonic increase in the BLUsH response as a function of estimated tissue CTZ concentration, a result that approximately tracks measurements of luminescent output as a function of [CTZ] *in vitro* (**Supplementary Figure 4**). Furthermore, repeated BLUsH signal increases with similar spatial profile can be elicited by injecting CTZ over multiple distinct cycles, with signal near the infusion site returning to baseline between injections (**Extended Data Fig. 7**). The mean peak amplitude for BLUsH signal following a single CTZ infusion was 4.0 ± 0.4% (**Figure 3g**), a significant response with Student's *t*-test $p = 0.006$ ($n = 5$). In contrast, control signal changes from luminescent cells in the absence of bPAC expression were negligible (*t*-test $p \geq 0.73$, $n = 3$). This indicates that responses to CTZ infusion could not be attributed to the infusion itself or to correlates of GLucM23 activity unrelated to light production, such as consumption of O_2 or generation of CO_2. Although CO_2 in particular can evoke hemodynamic signal increases under our imaging conditions (**Supplementary Figure 5**), such responses are absent from our bPAC-free controls.

BLUsH imaging of optical reporter expression in the brain. Bioluminescent reporters expressed directly in brain cells can be used to monitor a variety of neural processes[35]. To assess whether BLUsH could enable such applications to be performed with spatial resolution in deep tissue, we tested that ability of BLUsH to visualize endogenous luciferase expression in virally transduced cells *in situ*. Light-sensitive and control brain regions were again established in individual animals using the dual AAV transduction approach of **Figures 2-3**. To express the luciferase reporter, a third AAV encoding HA-tagged GLucM23 was co-administered with the BLUsH or control treatments.

BLUsH imaging was performed using MRI six weeks after viral injection. To achieve unbiased detection of luciferase activity throughout the brain, CTZ was administered systemically via the tail vein. Responses in the area of viral treatment were observed in BLUsH but not control animals (**Figure 4a** and **Extended Data Figs. 8-9**). Peak signal changes were observed up to 25 minutes after CTZ injection and declined with an average half time of 4.1 min (95% confidence interval = 3.2 to 5.5 min) (**Figure 4b**). The mean amplitude of peak signal change observed in BLUsH experiments was 6.7 ± 1.4% (significant with *t*-test $p = 0.0004$, $n = 5$), whereas the average peak signal change in control regions was 1.4 ± 0.6% ($p = 0.05$, $n = 3$) (**Figure 4c**).

Notably, patterns of MRI signal change following intravenous CTZ delivery approximately corresponded to luminescent reporter expression patterns at the level of individual BLUsH animals but not controls (**Figure 4d,e** and **Extended Data Fig. 10**), demonstrating the robustness of the visualization. To quantify this correspondence, we registered histological and MRI data into a common space and compared results on a voxel level after smoothing. The correlation coefficient between BLUsH and immunohistochemical fluorescence levels was 0.64 across 226 voxels in three animals, a significant correlation with $p < 10^{-4}$ (**Figure 4g**). An approximately linear relationship between luciferase expression and BLUsH signal was consistent, with similar slopes and intercepts across animals (**Figure 4h**). These results therefore

demonstrate that BLUsH yields accurate, spatially resolved measurements of endogenously expressed luminescent reporters in opaque brain tissue.

Discussion

Surpassing current limitations of optical imaging is a major goal in biotechnology development, and strategies for mapping light in deep tissue are particularly sought after[36]. The BLUsH approach achieves this by converting cerebral vessels into photodetectors, in effect turning the tissue itself into a near-field biological camera. We applied BLUsH in the brain, where inter-vessel spacing is on the order of cellular dimensions, but in principle BLUsH could be utilized in other areas as well. To detect BLUsH-based responses we used MRI, which is known for its unlimited coverage and depth penetration, as well as sensitivity to a variety of vascular and complementary nonvascular contrast mechanisms. We show that MRI-based BLUsH imaging can be used to image luminescent implanted cells and virally induced endogenous luciferase expression in opaque, anatomically defined contexts, revealing three-dimensional distributions of luminescent probe expression that are difficult to measure using stand-alone optical techniques in deep tissue.

The photon sensitivity of BLUsH arises from multiple enzymatic amplification factors, including the light-dependent actuator bPAC and downstream signal transduction components that directly drive VSMC relaxation and vasodilation. The dynamic range and linearity of BLUsH detection can be further characterized in specific applications. Data presented here suggest that a range of luminescent cell densities can be distinguished, but additional experiments could be applied to assess hemodynamic response properties in different tissue types or brain regions. Although vascular physiology could in principle be affected by O_2 consumption or CO_2 generation associated with luciferase activity, we did not observe evidence of this in any of our control measurements. This is indicates that luciferase-catalysed gas perturbations are too subtle to cause substantial hemodynamic responses on their own, consistent with the fact that the CTZ stoichiometry of our experiments predicts peak gas changes far below basal rates reported in rat brain[37]. On the other hand, we cannot entirely rule out unpredicted pathways for BLUsH signal generation that still rely on bPAC activation. A drawback of our vessel-dependent optical imaging strategy is that it obeys slower kinetics that most electronic or chemical light detectors. Nevertheless, response times of the BLUsH mechanism were shown to be on the order of seconds, meaning that time-resolved measurements from luminescent reporters could be possible on this temporal scale.

Spatially, resolution of the BLUsH technique is enhanced when using blue light emitters such as GLucM23, because their short wavelength output is more restricted to sites of reporter activity in tissue. The requirement for close proximity between luminescent cells and photosensitized vessels thus serves to improve spatial resolution. We found that BLUsH resolved the dimensions of cell implants and the distribution of endogenous luciferase expression, suggesting that the resolution of BLUsH images is well under 1 mm and likely limited by the in-plane MRI voxel dimension of 400 μm. The correlation between BLUsH and histology data in **Figure 4** was highly statistically significant but probably limited to some extent by resolution differences, misalignment between the MRI and histology slices, contributions from background fluorescence, and the fact that underlying signal sources in MRI and histology are different. A more advanced assessment could be performed by comparing MRI-based visualizations with volumetric histology data sets, possibly obtained from cleared tissue[38].

Equally important for future studies will be strategies for more uniform photosensitization of blood vessels than we have used for our initial BLUsH experiments here. This is particularly necessary for comprehensive mapping of luminescent reporters, given the requirement for spatial proximity of luciferase-expressing cells to photosensitized blood vessels. Uniform vessel sensitization could leverage minimally invasive gene delivery methods[39] or transgenic animals to express bPAC variants or alternative actuators[40] throughout large fields of view. This kind of approach could also go further to limit off-target expression of the photosensitizer, which we observed to some extent in our experiments. We showed that intraventricular injection of a Cre-dependent bPAC vector into an SM22□-Cre transgenic mouse can indeed result in homogeneous and specific vascular expression across the brain, which could be essential for future applications. Compared with the current studies, spatial precision of subsequent BLUsH measurements might be further refined by using single vessel-level imaging[41-43] to estimate luminescence patterns at finer scale via tomographic reconstruction methods. The success of such strategies could depend on specifics of vascular distribution in different tissues.

Extensions of the BLUsH technique can include its generalization to detection of additional luminescent reporters, including chemiluminescent probes and alternative luciferases that sense cell signalling or other biological events[35]. Future applications could employ luciferin analogs engineered for better blood-brain barrier permeability or for multiplexed parallel detection of luciferase variants with different substrate selectivity[44]. BLUsH might even be adapted to permit detection of fluorophores, where unfocused excitation light could be delivered through scattering tissue, but high resolution near-field imaging would be again performed using photosensitized blood vessels. Meanwhile, BLUsH detection could be performed using

alternative deep tissue imaging methods with complementary strengths, such as MRI with cerebral blood volume[45] or arterial spin labeling[46] contrast, functional ultrasound[47], photoacoustic tomography[48], and high-resolution hemodynamic X-ray imaging methods[49, 50]. With developments such as these, the BLUsH approach will permit the facile combination of diverse optical probes with virtually any imaging modality, on a scale that spans entire organs and organisms.

Methods

Plasmids. Codon-adapted synthetic genes encoding bPAC, GLucM23, sbGLuc and NanoLuc were purchased from Integrated DNA Technologies (Coralville, IA). All plasmids for expression in bacterial and mammalian cells were constructed using the Golden Gate method[51] in pEF-ENTR A (Addgene #17427, Watertown, MA) or gWiz backbones (Genlantis, San Diego, CA). Plasmids were produced in *Escherichia coli* (E. cloni 10G, Lucigen Corporation, Middleton, WI) grown in Lysogeny Broth media supplemented with kanamycin. Plasmids for adeno-associated virus (AAV) production were generated by Virovek (Hayward, CA) using respective synthetic genes.

Mammalian cell culture. CHO K1 cells and A7r5 vascular smooth muscle cells were purchased from MilliporeSigma (Burlington, MA) and cultured in 90% F10 or DMEM medium supplemented with 10% fetal bovine serum (FBS), 100 units/mL penicillin, and 100 µg/mL streptomycin. HEK 293 FreeStyle cells were purchased from Thermo Fisher Scientific (Waltham, MA) and grown in FreeStyle expression medium. Cells were frozen in freezing medium composed of 80% F10 medium, 10% FBS and 10% dimethylsulfoxide.

Lentivirus production and cell line generation. 293FT cells (Thermo Fisher) were seeded into six-well plates at 1 million cells per well and transfected using Lipofectamine 2000 (Life Technologies, Grand Island, NY) according to instructions at sub-confluence. Cotransfection of 0.5 mg pMD2.G, 1 mg psPAX2 and 1 mg of the previously described lentiviral plasmid[14] encoding Glo22F reporter[52] (Promega, Madison, WI) was performed with 6.25 mL Lipofectamine 2000 reagent. Virus-containing supernatant was collected after 48 and 72 h, filtered through 0.45 mm filters, and used for infection. Supernatants were stored at 4 °C for up to a week. A7r5 cells were seeded into 24-well plates at 5,000 cells per well in the presence of 4 μg/mL Polybrene in 50% fresh medium and 50% viral supernatants containing Glo22F virus. The medium was replaced with fresh viral supernatants daily for four days. Selection was performed using both antibiotic resistance and fluorescent markers for each lentivirus. Beginning on day 3 after initial infection, 10 mg/mL blasticidin and 1 mg/mL puromycin (Life Technologies) were added to the medium for selection and selection was continued until all cells expressed the appropriate fluorescent markers.

***In vitro* characterization of luciferases.** Testing of luciferases in bacteria was conducted by growing *Escherichia coli* BL21 (MilliporeSigma, Burlington, MA) transformed with respective luciferase-encoding plasmids in LB media supplemented with kanamycin at 37 °C to an optical density at 600 nm (OD_{600}) of 0.4. Expression of luciferase genes was induced by adding 1 mM isopropyl β-d-1-thiogalactopyranoside (IPTG) and cultures were grown over night at 16 °C. Samples of similar cell density (250,000 cells in 200 μL) were taken for all cultures and transferred to 96-well plates. Bioluminescence was stimulated by addition of 10 μL of 2 mM coelenterazine (CTZ) (#3031, CTZ-SOL, Nanolight Technology, Aurora, CO) to a final concentration of 95 μM, or by addition of varying amounts for titration analysis. Resulting bioluminescence was recorded using a microwell luminescence reader, a power meter, or IVIS Spectrum bioluminescent imaging system (Perkin Elmer, Waltham, MA). Testing in mammalian cells was conducted by transfecting HEK 293 FreeStyle cells with luciferase-encoding plasmids using 293fectin transfection reagent (Thermo Fisher). Luminescence was stimulated and measured as described above.

Lentivirus production and cell line generation. Lentivirus production and cell line generation. 293FT cells were seeded into six-well plates at 1 million cells per well and transfected using Lipofectamine 2000 (Life Technologies, Grand Island, NY) according to instructions at sub-confluence. Co-transfection of 0.5 mg pMD2.G, 1 mg psPAX2 and 1 mg of the lentiviral plasmid of interest was performed with 6.25 mL Lipofectamine 2000 reagent. Virus-containing supernatant was collected after 48 and 72 h, filtered through 0.45-mm filters, and used for infection. Supernatants were stored at 4 °C for up to a week. A7r5 cells were seeded into 24-well plates at 10,000 cells per well in the presence of 4 mg/mL Polybrene in 50% fresh medium and 50% viral supernatants containing the Glo22F virus. The medium was replaced with fresh viral supernatants daily for four days. Selection was performed using both antibiotic resistance and fluorescent markers for each lentivirus. Beginning on day 3 after initial infection, 10 mg/mL blasticidin and 1 mg/mL puromycin (Life Technologies) were added to the medium for selection and selection was continued until all cells expressed the fluorescent markers.

cAMP cell assay. Production of intracellular cAMP was measured using the GloSensor assay[52] (Promega) in CHO K12 or A7r5 cells. 48 hours before the assay 5000 CHO cells or 2000 A7r5 per well were seeded in 100 μL F10 or DMEM with 10% FBS in white opaque clear-bottom 96-well plates (Costar, Coppell, TX). After 24 hours, cells were transfected with bPAC-encoding plasmids using Lipofectamine (Thermo Fisher). Before the assay the medium was removed from the wells and replaced with 90 μL per well of Gibco CO_2-independent medium (Life Technologies) with 10% FBS containing 2% v/v of cAMP GloSensor substrate stock solution (Promega). The cells were incubated in substrate-containing medium at 37 °C in 5% CO_2 for 2-4 h and equilibrated to room temperature and atmospheric CO_2 for 30 min. Luminescence was measured for 30 min using a microtiter plate reader and evaluated after the signal reached a plateau (15 min). Dose–response curves were fitted to a four-parameter Hill equation using Prism (GraphPad Software, San Diego, CA). EC_{50} values are reported as mean and standard deviation of duplicate measurements.

Animal procedures. All animal procedures were conducted in accordance with National Institutes of Health guidelines and with the approval of the MIT Committee on Animal Care (protocol number 0721-059-24). All rat experiments were performed with male Sprague-Dawley animals, 300-400 g, supplied by Charles River Laboratories (Wilmington, MA). 26 rats were used for *in vivo* imaging experiments described here.

Intracranial injection of viral vectors. Adeno-associated viruses AAV9-SM22α-Cre-2A-GFP, AAV9-FLEX-CAG-bPAC-Myc-2A-mCherry, AAV9-CAG-GLucM23-HA were custom orders from Virovek. AAV9-CAG-FLEX-tdTomato was purchased from Addgene (#28306). Animals were anesthetized with isoflurane (4% for induction, 2% for maintenance) and positioned in a stereotaxic instrument (Kopf Instruments, Tujunga, CA) with a water heating pad (Braintree Scientific, Braintree, MA) to keep the body temperature at 37 °C. The animals' eyes were covered with Paralube Vet Ointment (Dechra Veterinary Products, Overland Park, KS) to prevent drying and the heads were shaved and cleaned with alcohol and povidone-iodine pads. Using sterile surgical equipment, the skin over the skull was retracted and the skull cleaned to expose target virus injection sites. Holes were drilled into the skull above the target sites, which were located in the cortex (AP +1 mm; ML ±2.5 mm, DV 0.5 mm) for imaging photosensitized vasculature or the central striatum (AP 0; ML ±3 mm, DV 5 mm) for BLUsH imaging of xenografts and optical reporter expression.

A glass pipette preloaded with appropriate viral vectors at final concentrations of 10^{12} vg/mL was lowered into the brain and viral vectors were injected into the brain parenchyma. Animals for imaging photosensitized vasculature and BLUsH imaging of xenografts were injected with a total volume of 1.5 μL of AAV9-SM22α-Cre-2A-GFP and AAV9-FLEX-CAG-bPAC-Myc-2A-mCherry at a 1:1 ratio. Animals for BLUsH imaging of optical reporter expression were injected with a total volume of 3 μL of AAV9-SM22α-Cre-2A-GFP, AAV9-FLEX-CAG-bPAC-Myc-2A-mCherry, and AAV9-CAG-GLucM23-HA at a 1:1:1 ratio. The glass pipette was slowly removed 10 min after the viral injection. Bone wax was applied to each injection site using a sterile cotton applicator tip. Skin incisions were closed using surgical suture and lidocaine gel (2%) was applied over the wound areas. Isoflurane was then discontinued, and each rat was removed from the stereotaxic frame and placed in a warmed cage on a heating pad to recover for 45 min. Slow-release buprenorphine (0.3 mg/kg, MIT Pharmacy) was administered subcutaneously to minimize pain and discomfort. To verify the feasibility of achieving brain-wide homogeneous bPAC expression, a small number of SM22α-Cre transgenic mice[53] (#017491, Jackson Laboratory, Bar Harbor, ME) underwent bilateral injection of 3 μL AAV.PHP.eB-FLEX-CAG- bPAC-Myc-2A-mCherry (Boston Children's Hospital, 6×10^{13} vg/mL) each into the ventricles, using procedures described above. Following standard practices in the field, a delay of six weeks between AAV infection and further experiments was instituted to allow AAV-mediated expression to develop.

Implantation of luminescent xenografts. HEK 293 FreeStyle cells transiently expressing GLucM23 as described above were harvested 48h after transfection, pelleted by centrifugation, washed with cold phosphate-buffered saline (PBS, pH 7.4) and resuspended at a density of 10^5 cells/μL in artificial cerebrospinal fluid (aCSF). Six weeks after viral injection (AAV9-SM22α-Cre-2A-GFP and AAV9-FLEX-CAG-bPAC-Myc-2A-mCherry or AAV9-FLEX-CAG-mCherry), immediately before the BLUsH experiment, GLucM23-expressing xenografts were intracranially implanted. Each animal was anesthetized, prepared for stereotaxic surgery and holes were drilled into the skull above the target sites (AP 0 mm, ML ±3 mm) as described above. 28 G PEEK cannula guides (Plastics One, Roanoke, VA) designed to project 1 mm below the surface of the skull were lowered through the holes. The guides were fixed in place using SEcure light-curing dental cement (Parkell, Brentwood, NY). A custom-fabricated plastic headpost was placed in front of the guide cannula and also secured with dental cement (Parkell). To deliver cells, 33 G metal internal cannulas (Plastics One) were lowered through the guide cannulas to a depth of 5.5 mm below the skull. Approximately 5×10^5 GLucM23-expressing cells (5 μL) were infused to the bPAC-expressing brain hemispheres, control hemispheres or naïve brain regions via the cannulas at a flow rate of 0.2 μL/min for 25

min. The internal cannulas were slowly removed 10 min after the infusion. Cannula guides were then sealed with dummy cannulas.

Functional MRI of photosensitized vasculature. Animals were anesthetized with isoflurane (4% for induction, 2% for maintenance). Small cranial windows of around 1 mm^2 were prepared above the respective virus injection sites, and over more caudal control sites where no virus was administered. Animals were then transferred to a 9.4 T MRI scanner (Bruker Instruments, Ettlingen, Germany) and fixed into a custom rat MRI cradle. Isoflurane was discontinued and animals sedated with intraperitoneal (IP) medetomidine (bolus of 0.1 mg/kg, followed by 0.1 mg/kg/h infusion). An optical fibre of 200 μm diameter coupled to a blue light emitting diode (LED, 470 nm from NPI Electronic) was mounted on top of each cranial window to provide light illumination with the output intensities of 0.1, 0.5, and 1.0 mW/cm^2, as measured using a light power meter at the fibre tip. Cranial windows were then sealed with silicone gel. A transmit-only 70-cm-inner-diameter linear volume coil (Bruker) and a three-channel surface receive-only radiofrequency coil (Bruker) were used for image acquisition.

Scanner operation was controlled using the ParaVision 6.1 software (Bruker). Field map shimming was performed to optimize main field homogeneity. High-resolution anatomical MRI images were acquired using a longitudinal relaxation time (T_2)-weighted rapid acquisition with refocused echoes (RARE) pulse sequence with RARE factor = 8, bandwidth = 200 kHz, effective echo time (TE) = 30 ms, repetition time (TR) = 5 s, in-plane field of view (FOV) = 2.56 × 2.56 cm^2, in-plane resolution of 100 × 100 μm^2 and slice thickness = 1 mm. Functional imaging scan series were acquired using a standard gradient echo echo-planar imaging (EPI) pulse sequence with TE values = 20 ms; flip angle = 90°, TR = 2 s, FOV = 2.56 × 2.56 cm^2 and in-plane resolution of 400 × 400 μm^2 with slice thickness = 1 mm. EPI MRI scans were continuously collected for 2 min of baseline, for 1 min during illumination, and for 7 min after illumination. Animals were warmed using a water heating pad (Braintree). Heart rate and blood oxygenation saturation level were continuously monitored using an MRI-compatible infrared pulse oximeter (Nonin Medical, Plymouth, MN). Breathing rate and CO_2 level were continuously monitored using an MRI-compatible SurgiVet CO_2 monitor (Smiths Medical, Minneapolis, MN).

MRI images were reconstructed using the ParaVision 6.1 software and further processed using the AFNI software package[54]. High-resolution anatomical images were registered based on the location of cranial windows at each stimulation site, such that all test or control stimulation sites were positioned on the righthand side after alignment, using left-right reflection where needed. Time series of T_2*-weighted EPI images were preprocessed in steps that included slice timing correction, motion correction using a least-squares rigid-body volume registration algorithm, voxel-wise intensity normalization, spatial smoothing with gaussian spatial kernel of 0.5 mm full-width at half maximum and spatial resampling to double the image matrix size, all implemented in AFNI. Segmentation of brain from nonbrain voxels was performed in MATLAB (Mathworks, Natick, MA). Preprocessed time series were then coregistered onto the previously aligned anatomical images. Response maps were computed as mean percent signal change during the expected peak response time point, 0-40 s after the onset of light illumination minus the average baseline signal 40-120 s before stimulus onset. Mean response maps from aligned stimulated hemispheres were overlaid on full coronal anatomical MRI slices to produce panels in Figure 2d.

Mean response amplitudes and time courses were evaluated over regions of interest (ROIs) defined with respect to fibre tips estimated from the MRI scans. Time courses were baseline corrected using the initial and final 50 time points and are presented as mean and SEM over animals. Amplitudes were defined as the mean percent signal change observed from 40-80 s after stimulus onset, with respect to baseline signal 20-60 s before onset. Depth profiles represent mean amplitudes measured at 200 μm depth increments from the fibre tip locations. Rate constants for response to and recovery from optical stimulation were estimated by fitting monoexponential curves to the first 120 s after stimulus onset or the first 360 s after stimulus offset, respectively.

BLUsH imaging of luminescent xenografts. After implantation of GLucM23-expressing cells, the internal metal cannulas were removed. Animals were then transferred to the scanner and placed in the cradle. 33 G PEEK internal cannulas (Plastics One) were connected to PE-50 tubing (Plastics One) loaded with coelenterazine (CTZ, 2 mM), and lowered through the guide cannulas to the same site for cells implantation, at a depth of 5.5 mm below the skull. Animals were anesthetized, sedated and monitored as described above and paralyzed with pancuronium (IP bolus of 1 mg/kg, followed by 1 mg/kg/h infusion). Intubation and ventilation were conducted with a small animal ventilator (Harvard Apparatus, Holliston, MA) which operated at 62 beats per minute with a 6-mL stroke volume, delivering oxygen and air as a 5:1 ratio mixture. General MRI methods, including hardware, anatomical imaging and functional T_2*-weighted imaging, were similar to those described above. EPI MRI scans were continuously collected for 5 min of baseline, for 5 min during

CTZ infusion and for 20 min of resting after the infusion. Intracranial CTZ infusion was produced by infusion of a 2 mM solution of CTZ in Ringer's solution, at a rate of 0.2 μL/min through the internal cannulas.

MRI images were reconstructed and preprocessed as described above. High-resolution anatomical images of each animal were registered to a Waxholm coordinate space rat brain atlas[55] using AFNI, again such that implant sites were positioned on the righthand side. MATLAB codes were used for the rest of the analysis. Response maps were computed as mean percent signal change during the expected peak response time point, 1-120 s after the onset of CTZ infusion minus the average baseline signal 20-200 s before infusion. Average response maps from xenografts in aligned hemispheres were overlaid on full coronal anatomical MRI slices to produce panels in **Figure 3b**.

Mean response amplitudes and time courses were evaluated over an ROI around the cell implantation area. These ROIs were defined by 1.6 mm × 1.2 mm regions of interest defined around cannula tip locations in individual animals' datasets and standard error was calculated across animals. Closeup average percent signal change and corresponding standard deviation maps were computed by combining data from 3.8 x 3.8 mm squares defined around the centroid of CTZ-induced MRI signal change in each experiment. Full-widths at half maximum were computed from interpolated cross sections at the dorsolateral median of each response. A model of the expected BLUsH signal through the median of a 1 mm-diameter spherical xenograft was generated by computing the one-dimensional projection of a circular cross-section and smoothing it by a gaussian function to simulate the MRI data processing.

CTZ dose response curves for the xenograft BLUsH experiments were generated by comparing effective CTZ concentrations to the mean MRI response amplitudes in volumes approximately corresponding to the closeup analysis of BLUsH signal changes in **Figure 3c**. Effective [CTZ] values were estimated by dividing the total injected amount of CTZ at varying time points by a 58 μL volume (11 × 11 × 3 voxels) centred around the centroid of maximal CTZ-induced MRI signal change in each experiment. Mean BLUsH response amplitudes were computed over the same volumes at the same time points used for [CTZ] estimation.

Consideration of CO_2 effects. To investigate responses to CO_2-induced vasodilation, two further animals underwent MRI at 7 T under conditions otherwise equivalent to the xenograft BLUsH experiments of **Figure 3**, but during challenge with inhaled carbogen (90% CO_2, 10% O_2) in place of CTZ injection. Response maps were computed as the percent difference between mean EPI signal in the 20 s after carbogen-induced monotonic signal increases versus mean signal in the 20 s prior to carbogen response. An estimated upper bound on CO_2 production and O_2 consumption rates in the xenograft experiments was based on the infusion parameters of 2 mM CTZ at 0.2 μL/min over 5 μL (~5 mg) of cells. Assuming optimistically that all CTZ is instantaneously converted, this implies O_2 consumption and CO_2 generation rates of 0.1 μmol/(g cells)/min.

BLI of luminescent xenografts. HEK 293 FreeStyle cells transiently expressing GLucM23 or the red-shifted luciferase Akaluc were harvested 48 h after transfection, pelleted by centrifugation, washed with cold phosphate-buffered saline (PBS, pH 7.4) and resuspended at a density of 10^5 cells/μL in aCSF. Luminescence of the cells when exposed to the substrates CTZ (for GLucM23) and the luciferin analogue Akalumine (for Akaluc) was confirmed by imaging transfected cells in a microtiter plate using a high-sensitivity camera (iXon Life 897 EMCCD, Andor USA, Concord, MA) in a custom-fabricated chamber. Four animals then underwent a craniotomy and approximately 5 × 10^5 luminescent cells were implanted into each animal via a 26-gauge Hamilton syringe at a flow rate of 0.2 μL/min for 25 min, targeting the same coordinates used for MRI studies. Two animals received GLucM23 cells and two received Akaluc cells. Using a Hamilton syringe, 8 μL of 5 mM CTZ or 8 μL of 6.2 mM Akalumine were infused at a rate of 2 μL/min over the corresponding implanted xenografts before withdrawal of the infusion needle. The scalp was sutured over the implantation site and animals were immediately imaged using the camera, with exposure parameters for GLucM23 of 100 gain with 1 s exposure, and for Akaluc of 100 gain with 30 s exposure. Values are presented as two-dimensional plots of luminescence in arbitrary units superimposed on brightfield images. FWHM values were computed from gaussian fitting of the cross section with brightest luminescence signal.

BLUsH imaging of virally driven optical reporter expression. MRI imaging was performed 6 weeks after viral injection. Animals were anesthetized, sedated and continuously monitored during imaging as described above. General MRI imaging hardware, anatomical imaging and functional T_2*-weighted imaging were the same as the section above. CTZ (250 μL at 2 mM) was administered systemically via the tail vein. EPI scans were continuously collected before, during and after the administration of CTZ. MRI images were reconstructed, preprocessed, and registered the same way as described above, with treatment sites all on the righthand side after alignment. Peak BLUsH MRI signals were observed up to 25 minutes after CTZ injection. Response maps were computed as mean percent signal change observed over a time window of 40 s starting at the peak signal change minus the average baseline signal observed 100-200 s before the

peak. Mean response amplitudes and time courses were evaluated over an ROI of 3 x 3 voxels around the maximum signal change. Peak signal changes were quantified as the maximal signal amplitude in each test and control animal with respect to an average baseline 100-200s before the peak signal.

Correspondence between BLUsH and histology images was assessed after aligning GLuc histology images from each of three animals to the corresponding single-slice BLUsH MRI images, as judged by eye. Affine alignment was performed using the *imwarp* command in MATLAB, with landmarks chosen manually around cortical features and ventricles. Data were smoothed along both dimensions with a gaussian of window size = 6.4 mm. Correlations and linear regression parameters were computed by comparing BLUsH signal amplitudes and normalized GLuc fluorescence (F/F_{max}) of the resulting aligned, smoothed images for each of the three animals.

Histology. Animals were transcardially perfused with PBS followed by 4% paraformaldehyde in PBS. Brains were extracted, post-fixed overnight at 4 °C, and sectioned the following day. Free-floating sections (50 μm thick) were cut using a vibratome (Leica VT1200 S, Leica Microsystems GmbH, Wetzlar, Germany). We performed antigen retrieval by incubating brain sections in sodium citrate buffer (pH 6) for 30 minutes at 80 °C.

Expression of bPAC, fluorescent control proteins, and GLucM23 were assessed by overnight incubation with primary antibodies Anti-mCherry (1:250 dilution, LS-C204207, Lifespan Biosciences, Seattle, WA), Anti-tdTomato (1:250 dilution, LS-C340696, Lifespan Biosciences, Seattle, WA) and Anti-HA (1:250 dilution, NB600-363, Novus Biologicals, Centennial, CO), followed by a one-hour incubation with matching secondary antibodies Anti-Goat Alexa Fluor 594 (1:500 dilution, ab150132, Abcam, Cambridge, UK) and Anti-Rabbit Alexa Fluor 405 (1:500 dilution, ab175651, Abcam, Cambridge, UK). Cell implants expressing GLucM23 were stained using Anti-His (1:250 dilution, MA5-33032, Invitrogen, Waltham, MA) primary and Anti-Rabbit Alexa Fluor 405 secondary antibodies.

Microglial activation in BLUsH brain slices was assessed using two-day incubation with primary antibodies Anti-mCherry (1:500 dilution, ab205402, Abcam, Cambridge, UK), Anti-HA (1:500 dilution, ab9110, Abcam, Cambridge, UK), and Anti-Iba1 (1:500 dilution, ab5076, Abcam, Cambridge, UK), followed by a three-hours incubation with matching secondary antibodies Anti-Chicken Alexa Fluor 647 (1:500 dilution, A78952, Invitrogen, Waltham, MA), Anti-Rabbit Rhodamine Red (1:200 dilution, 711-295-152, Jackson ImmunoResearch, West Grove, PA), and Anti-Goat Alexa Fluor 488 (1:500 dilution, 705-545-003, Jackson ImmunoResearch, West Grove, PA). Inflammation markers were assessed using Anti-Nitrotyrosine (1:200 dilution, MilliporeSigma AB5411) with secondary antibody Anti-Rabbit Alexa Fluor 405 (1:500 dilution, ab175651, Abcam, Cambridge, UK). Vascular staining was performed by overnight incubation of brain sections with Tomato Lectin DyLight488 (1:250 dilution, DL-1174, Vector Laboratories, Burlingame, CA).

Stained brain sections were mounted on glass slides with Invitrogen ProLong Gold Antifade (Fisher Scientific Company, Ottawa, Canada) and protected with a coverslip. Fluorescence imaging was performed using a confocal microscope (Axio Imager 2, Zeiss, Thornwood, NY).

Reporting Summary. Further information on research design is available in the Nature Research Reporting Summary linked to this article.

Data availability

The main data supporting the results in this study are available within the paper and its Supplementary Information. The MRI atlas used for this study was downloaded from https://www.nitrc.org/projects/whs-sd-atlas.

References

1. Yeh, H.W. & Ai, H.W. Development and Applications of Bioluminescent and Chemiluminescent Reporters and Biosensors. *Annu Rev Anal Chem (Palo Alto Calif)* **12**, 129-150 (2019).
2. Liu, S., Su, Y., Lin, M.Z. & Ronald, J.A. Brightening up Biology: Advances in Luciferase Systems for in Vivo Imaging. *ACS Chem Biol* **16**, 2707-2718 (2021).
3. Dothager, R.S. et al. Advances in bioluminescence imaging of live animal models. *Curr Opin Biotechnol* **20**, 45-53 (2009).
4. Tung, J.K., Berglund, K., Gutekunst, C.A., Hochgeschwender, U. & Gross, R.E. Bioluminescence imaging in live cells and animals. *Neurophotonics* **3**, 025001 (2016).
5. Tian, X. et al. A luciferase prosubstrate and a red bioluminescent calcium indicator for imaging neuronal activity in mice. *Nat Commun* **13**, 3967 (2022).
6. Wang, G., Li, Y. & Jiang, M. Uniqueness theorems in bioluminescence tomography. *Med Phys* **31**, 2289-2299 (2004).

7. Gu, X., Zhang, Q., Larcom, L. & Jiang, H. Three-dimensional bioluminescence tomography with model-based reconstruction. *Opt Express* **12**, 3996-4000 (2004).
8. Tu, C. & Louie, A.Y. Photochromically-controlled, reversibly-activated MRI and optical contrast agent. *Chem Commun (Camb)*, 1331-1333 (2007).
9. Osborne, E.A., Jarrett, B.R., Tu, C. & Louie, A.Y. Modulation of T2 relaxation time by light-induced, reversible aggregation of magnetic nanoparticles. *J Am Chem Soc* **132**, 5934-5935 (2010).
10. Venkataramani, S. et al. Magnetic bistability of molecules in homogeneous solution at room temperature. *Science* **331**, 445-448 (2011).
11. Hai, A., Spanoudaki, V.C., Bartelle, B.B. & Jasanoff, A. Wireless resonant circuits for the minimally invasive sensing of biophysical processes in magnetic resonance imaging. *Nat Biomed Eng* **3**, 69-78 (2019).
12. Reessing, F. et al. A light-responsive liposomal agent for MRI contrast enhancement and monitoring of cargo delivery. *Chem Commun (Camb)* **55**, 10784-10787 (2019).
13. Simon, J., Schwalm, M., Morstein, J., Trauner, D. & Jasanoff, A. Mapping light distribution in tissue by using MRI-detectable photosensitive liposomes. *Nat Biomed Eng* (2022).
14. Ohlendorf, R. et al. Target-responsive vasoactive probes for ultrasensitive molecular imaging. *Nat Commun* **11**, 2399 (2020).
15. Desai, M., Slusarczyk, A.L., Chapin, A., Barch, M. & Jasanoff, A. Molecular imaging with engineered physiology. *Nat Commun* **7**, 13607 (2016).
16. Desai, M. et al. Hemodynamic molecular imaging of tumor-associated enzyme activity in the living brain. *Elife* **10** (2021).
17. Ghosh, S. et al. Functional dissection of neural circuitry using a genetic reporter for fMRI. *Nat Neurosci* **25**, 390-398 (2022).
18. Ji, X. et al. Brain microvasculature has a common topology with local differences in geometry that match metabolic load. *Neuron* **109**, 1168-1187 e1113 (2021).
19. Farhadi, A., Sigmund, F., Westmeyer, G.G. & Shapiro, M.G. Genetically encodable materials for non-invasive biological imaging. *Nat Mater* **20**, 585-592 (2021).
20. Attwell, D. et al. Glial and neuronal control of brain blood flow. *Nature* **468**, 232-243 (2010).
21. Walsh, M.P. & Cole, W.C. The role of actin filament dynamics in the myogenic response of cerebral resistance arteries. *J Cereb Blood Flow Metab* **33**, 1-12 (2013).
22. Hillman, E.M. Coupling mechanism and significance of the BOLD signal: a status report. *Annu Rev Neurosci* **37**, 161-181 (2014).
23. Stierl, M. et al. Light modulation of cellular cAMP by a small bacterial photoactivated adenylyl cyclase, bPAC, of the soil bacterium Beggiatoa. *J Biol Chem* **286**, 1181-1188 (2011).
24. Berglund, K. et al. Combined Optogenetic and Chemogenetic Control of Neurons. *Methods Mol Biol* **1408**, 207-225 (2016).
25. Hall, M.P. et al. Engineered luciferase reporter from a deep sea shrimp utilizing a novel imidazopyrazinone substrate. *ACS Chem Biol* **7**, 1848-1857 (2012).
26. Park, S.Y. et al. Novel luciferase-opsin combinations for improved luminopsins. *J Neurosci Res* **98**, 410-421 (2020).
27. Stuven, B. et al. Characterization and engineering of photoactivated adenylyl cyclases. *Biol Chem* **400**, 429-441 (2019).
28. Moessler, H. et al. The SM 22 promoter directs tissue-specific expression in arterial but not in venous or visceral smooth muscle cells in transgenic mice. *Development* **122**, 2415-2425 (1996).
29. Chakraborty, R. et al. Promoters to Study Vascular Smooth Muscle. *Arterioscler Thromb Vasc Biol* **39**, 603-612 (2019).
30. Deverman, B.E. et al. Cre-dependent selection yields AAV variants for widespread gene transfer to the adult brain. *Nat Biotechnol* **34**, 204-209 (2016).
31. Han, S., Son, J.P., Cho, H., Park, J.Y. & Kim, S.G. Gradient-echo and spin-echo blood oxygenation level-dependent functional MRI at ultrahigh fields of 9.4 and 15.2 Tesla. *Magn Reson Med* **81**, 1237-1246 (2019).
32. Grandjean, J. et al. A consensus protocol for functional connectivity analysis in the rat brain. *Nat Neurosci* **26**, 673-681 (2023).
33. Abe, Y. et al. Optical manipulation of local cerebral blood flow in the deep brain of freely moving mice. *Cell Rep* **36**, 109427 (2021).
34. Iwano, S. et al. Single-cell bioluminescence imaging of deep tissue in freely moving animals. *Science* **359**, 935-939 (2018).
35. Wang, A., Feng, J., Li, Y. & Zou, P. Beyond Fluorescent Proteins: Hybrid and Bioluminescent Indicators for Imaging Neural Activities. *ACS Chem Neurosci* **9**, 639-650 (2018).
36. Ntziachristos, V. Going deeper than microscopy: the optical imaging frontier in biology. *Nat Methods* **7**, 603-614 (2010).

37. Wiesner, H.M. et al. Quantitative and simultaneous measurement of oxygen consumption rates in rat brain and skeletal muscle using (17) O MRS imaging at 16.4T. *Magn Reson Med* **85**, 2232-2246 (2021).
38. Ueda, H.R. et al. Tissue clearing and its applications in neuroscience. *Nat Rev Neurosci* **21**, 61-79 (2020).
39. Bedbrook, C.N., Deverman, B.E. & Gradinaru, V. Viral Strategies for Targeting the Central and Peripheral Nervous Systems. *Annu Rev Neurosci* **41**, 323-348 (2018).
40. Rost, B.R., Schneider-Warme, F., Schmitz, D. & Hegemann, P. Optogenetic Tools for Subcellular Applications in Neuroscience. *Neuron* **96**, 572-603 (2017).
41. Yu, X. et al. Sensory and optogenetically driven single-vessel fMRI. *Nat Methods* **13**, 337-340 (2016).
42. Renaudin, N. et al. Functional ultrasound localization microscopy reveals brain-wide neurovascular activity on a microscopic scale. *Nat Methods* **19**, 1004-1012 (2022).
43. Zhu, X. et al. Real-time whole-brain imaging of hemodynamics and oxygenation at micro-vessel resolution with ultrafast wide-field photoacoustic microscopy. *Light Sci Appl* **11**, 138 (2022).
44. Zambito, G., Chawda, C. & Mezzanotte, L. Emerging tools for bioluminescence imaging. *Curr Opin Chem Biol* **63**, 86-94 (2021).
45. Belliveau, J.W. et al. Functional cerebral imaging by susceptibility-contrast NMR. *Magn Reson Med* **14**, 538-546 (1990).
46. Williams, D.S., Detre, J.A., Leigh, J.S. & Koretsky, A.P. Magnetic resonance imaging of perfusion using spin inversion of arterial water. *Proc Natl Acad Sci U S A* **89**, 212-216 (1992).
47. Mace, E. et al. Functional ultrasound imaging of the brain. *Nat Methods* **8**, 662-664 (2011).
48. Wang, L.V. & Hu, S. Photoacoustic tomography: in vivo imaging from organelles to organs. *Science* **335**, 1458-1462 (2012).
49. Hayasaka, N. et al. In vivo diagnostic imaging using micro-CT: sequential and comparative evaluation of rodent models for hepatic/brain ischemia and stroke. *PLoS One* **7**, e32342 (2012).
50. Starosolski, Z. et al. Ultra High-Resolution In vivo Computed Tomography Imaging of Mouse Cerebrovasculature Using a Long Circulating Blood Pool Contrast Agent. *Sci Rep* **5**, 10178 (2015).
51. Engler, C., Kandzia, R. & Marillonnet, S. A one pot, one step, precision cloning method with high throughput capability. *PLoS One* **3**, e3647 (2008).
52. Fan, F. et al. Novel genetically encoded biosensors using firefly luciferase. *ACS Chem Biol* **3**, 346-351 (2008).
53. Holtwick, R. et al. Smooth muscle-selective deletion of guanylyl cyclase-A prevents the acute but not chronic effects of ANP on blood pressure. *Proc Natl Acad Sci U S A* **99**, 7142-7147 (2002).
54. Cox, R.W. AFNI: software for analysis and visualization of functional magnetic resonance neuroimages. *Comput Biomed Res* **29**, 162-173 (1996).
55. Papp, E.A., Leergaard, T.B., Calabrese, E., Johnson, G.A. & Bjaalie, J.G. Waxholm Space atlas of the Sprague Dawley rat brain. *Neuroimage* **97**, 374-386 (2014).

Acknowledgements
The authors acknowledge grants to A.J. from the National Institutes of Health (UG3 MH126868, U01 EB031641, R21 EY032369, and R01 NS121073) and the G. Harold and Leila Y. Mathers Foundation. They also gratefully acknowledge research funding from Lore McGovern, Gardner Hendrie, and Brendan Fikes. R.O. was funded by a fellowship from the Deutsche Forschungsgemeinschaft. M.S. was funded by a Marie Skłodowska-Curie fellowship from the European Union. Y.K. was supported by a Y. Eva Tan Fellowship and Y.J. was supported by a J. Douglas Tan Fellowship, both from the McGovern Institute for Brain Research. Andrew Becker and Kyle Backman are thanked for technical support.

Author contributions
R.O. and A.J. designed the BLUsH principle. R.O. performed most of the *in vitro* experiments. N.L. and R.O. performed the *in vivo* MRI experiments with contributions from V.D.P.V., M.S., M.D., and W.T.Z. R.O., V.D.P.V., Y.K., and B.S. performed histology analyses. Y.K. and Y.J. performed the BLI experiments. S.D. performed the *in vitro* CTZ titration. N.L., R.O., and A.J. analysed the imaging data. R.O., N.L., and A.J. wrote the manuscript.

Competing interests
The other authors declare no competing interests.

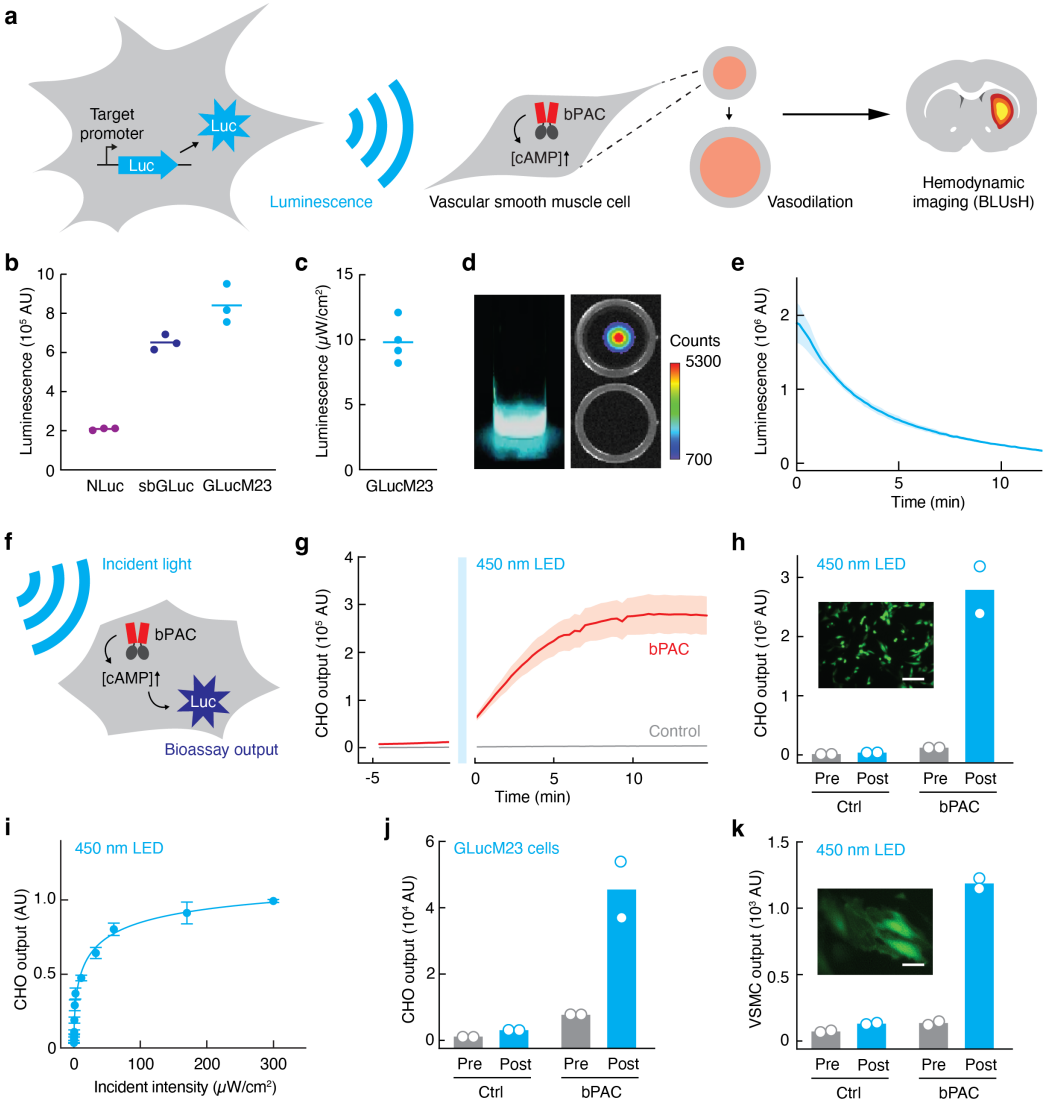

Fig. 1 | Characterization of BLUsH components. (a) In the BLUsH mechanism, vascular smooth muscle cells are photosensitized by expression of the light-activated adenylate cyclase bPAC. Light emission by cells expressing luciferase reporters (blue) triggers bPAC-mediated vasodilation and subsequent hemodynamic imaging signals. **(b)** Comparison of luminescence output of three luciferases. **(c)** Quantification of peak light output by GLucM23-expressing HEK cells (~250,000 cells per measurement). **(d)** Visualization of luminescent cells (left) and measurement in a standard BLI system (right). **(e)** Time course of bioluminescence signal from HEK cells expressing GLucM23, following addition of a single dose of CTZ; shading denotes SD of three biological replicates. **(f)** Schematic of a bioassay for measuring blue light-dependent bPAC activation via activation of a cAMP-sensitive luminescent reporter. **(g)** CHO cell-based bioassay results comparing LED stimulation of bPAC-expressing (red) *vs.* control cells (grey). Shading denotes SD of three biological replicates. **(h)** Amplitudes of signal observed in the CHO bioassay before (grey) and after (blue) LED stimulation. Inset: CHO bioassay cells (green) with scale bar (100 μm). **(i)** CHO bioassay output as a function of LED stimulation intensity. Data point denote mean values and error bars SD of three biological replicates. **(j)** CHO bioassay output before (grey) and after (blue) stimulation by exposure to GLucM23-expressing HEK cells (250,000 cells at ~15 mm distance). **(k)** Reporter output from VSMCs expressing bioassay components before (grey) and after (blue) LED stimulation as in panels g-h. Inset: VSMC bioassay cells (green) with scale bar (100 μm).

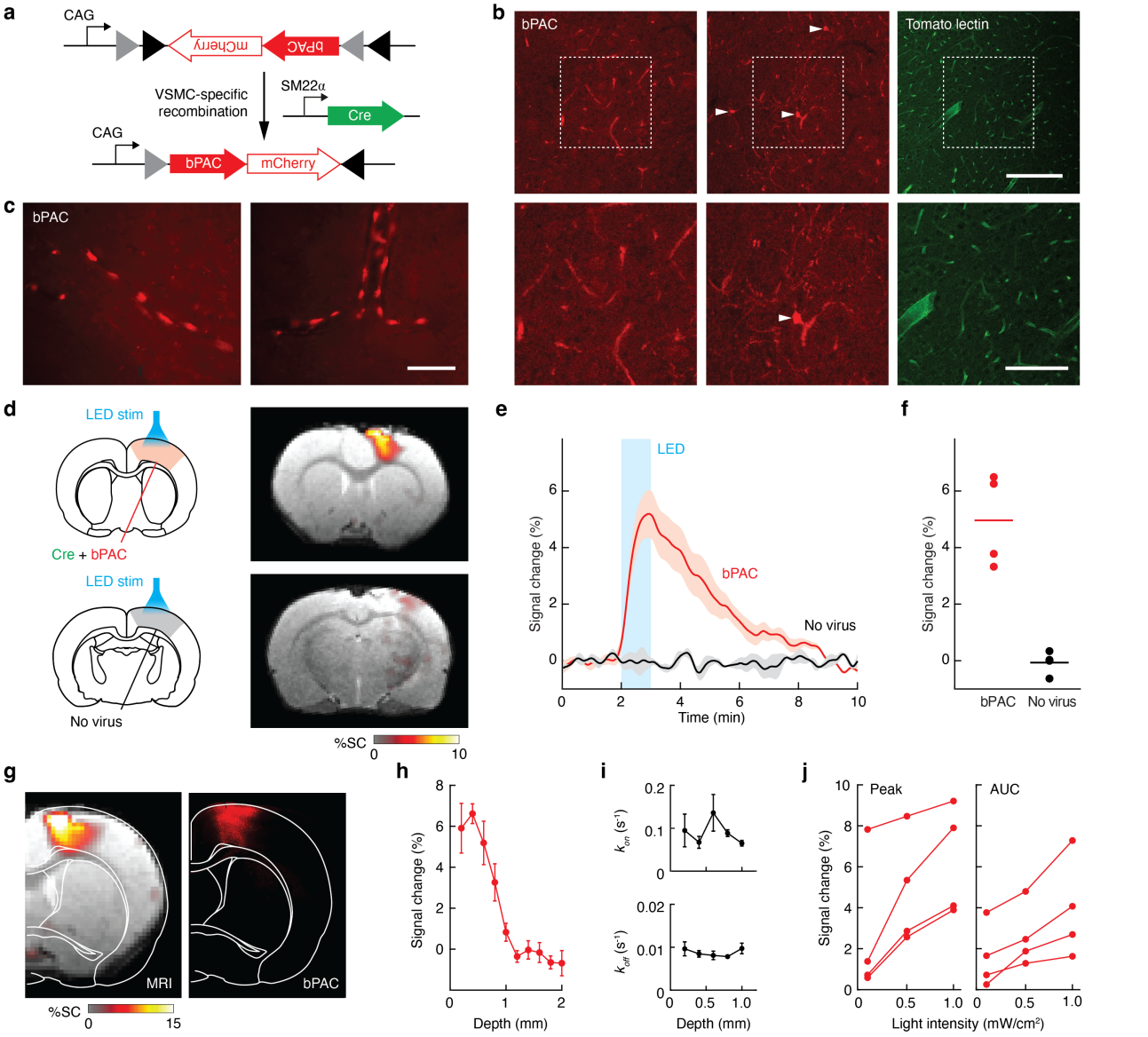

Fig. 2 | Evaluation of photosensitized vasculature. (a) VSMC-restricted expression is achieved by delivering a Cre-activatable AAV encoding bPAC flanked by loxP sites (arrowheads) (top) in combination with a second AAV encoding Cre under control of the VSMC-specific SM22α promoter (right), resulting in constitutive expression of bPAC (bottom). **(b)** Vascular expression profile confirmed by comparing bPAC expression patterns in two fields of view (red) with tomato lectin vascular staining in a different animal (green). Arrowheads indicate labelled structures with neuronal morphology, possibly reflecting off-target bPAC expression. Scale bars: 200 μm (top) and 100 μm (bottom). **(c)** Images showing bPAC expression in individual cells spaced along large individual vessels. Scale bar = 100 μm. **(d)** Mean fMRI responses to fibre-mediated light stimulation schematized at left in BLUsH-treated (top) *vs.* control (bottom) brain sites ($n = 4$ each). **(e)** Time courses of signal change in response to LED stimulation (blue rectangle) in BLUsH (red) and control (purple) conditions. Shading denotes SEM of four measurements. **(f)** Peak response amplitudes observed in the experiments of d-e. **(g)** Correspondence of a BLUsH response profile (left) with bPAC expression visualized by histology (right). **(h)** Responses to 1 mW/cm^2 stimulation as a function of depth from fibre tip. Error bars are SEM of $n = 4$. **(i)** On (top) and off (bottom) rates of BLUsH responses as a function of depth. Error bars are SEM of $n = 4$. **(j)** BLUsH responses to varying light intensity in four experiments. Peak signal (left) and integrated area under the curve (AUC, right) are both shown.

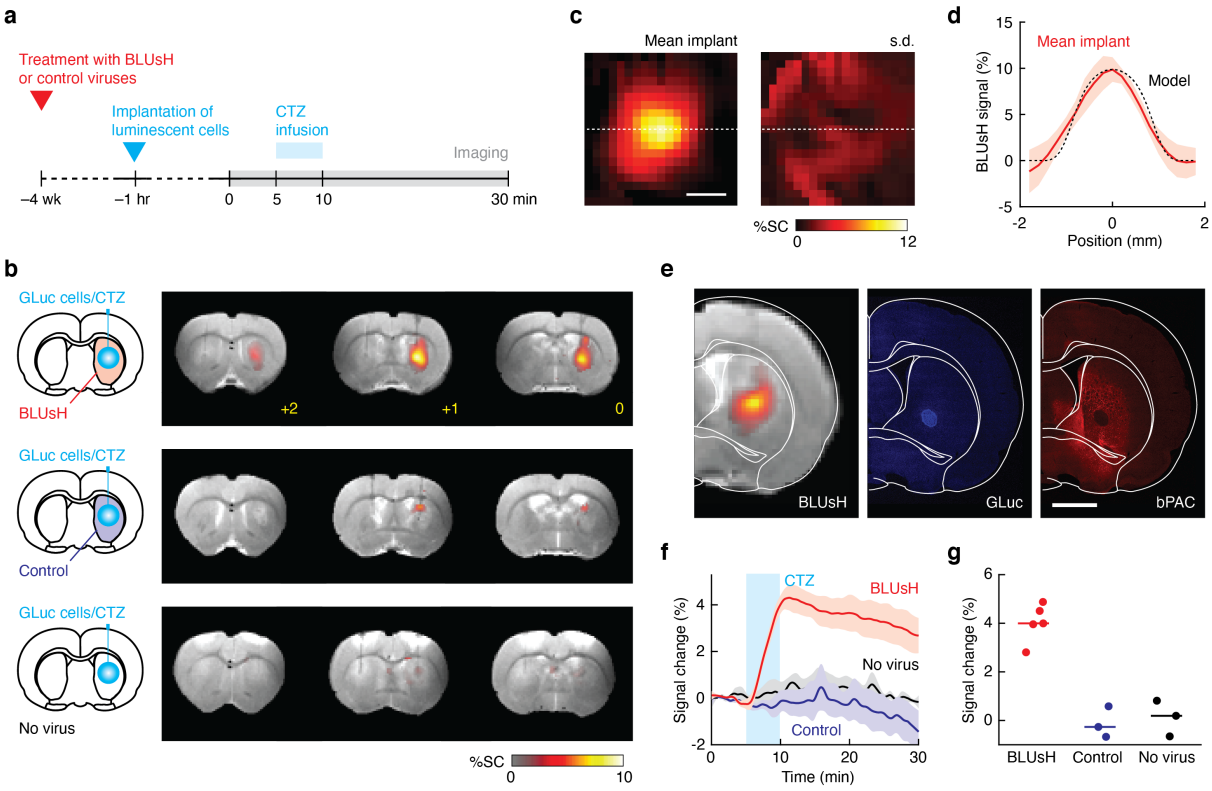

Fig. 3 | Deep-brain BLUsH imaging of luminescent xenografts. (a) Timeline of experiments showing viral infection time (red arrowhead), cell implantation (blue arrowhead), imaging (grey bar), and CTZ infusion period (blue rectangle). **(b)** Average results from xenograft imaging with BLUsH (top, $n = 5$), in the presence of a control virus (middle, $n = 3$), and in untreated brain tissue (bottom, $n = 3$). Schematics at left diagram experimental conditions. Bregma coordinates in yellow. **(c)** Closeup of mean signal from BLUsH xenograft imaging (left) with SD over five experiments shown on the same colour scale (right) to indicate consistency of the results. Scale bar = 1 mm. **(d)** Comparison of mean BLUsH signal (red line, shading = SD of $n = 5$) with a model profile expected from a 1 mm implant (black dashed line). The BLUsH curve corresponds to a cross section through the image in c (white dashed line). **(e)** Comparison of BLUsH and histology data from a representative animal. Scale bar = 2 mm. **(f)** Signal time courses showing signal changes elicited by CTZ delivery (blue rectangle) in BLUsH imaging (red), control virus-treated tissue (purple), and untreated tissue (black). Shading = SEM of five (BLUsH) or three (controls) biological replicates. **(g)** Peak signal changes observed following CTZ delivery in BLUsH and control experiments. Lines indicate average peak signal changes and dots values of single biological replicates for each group.

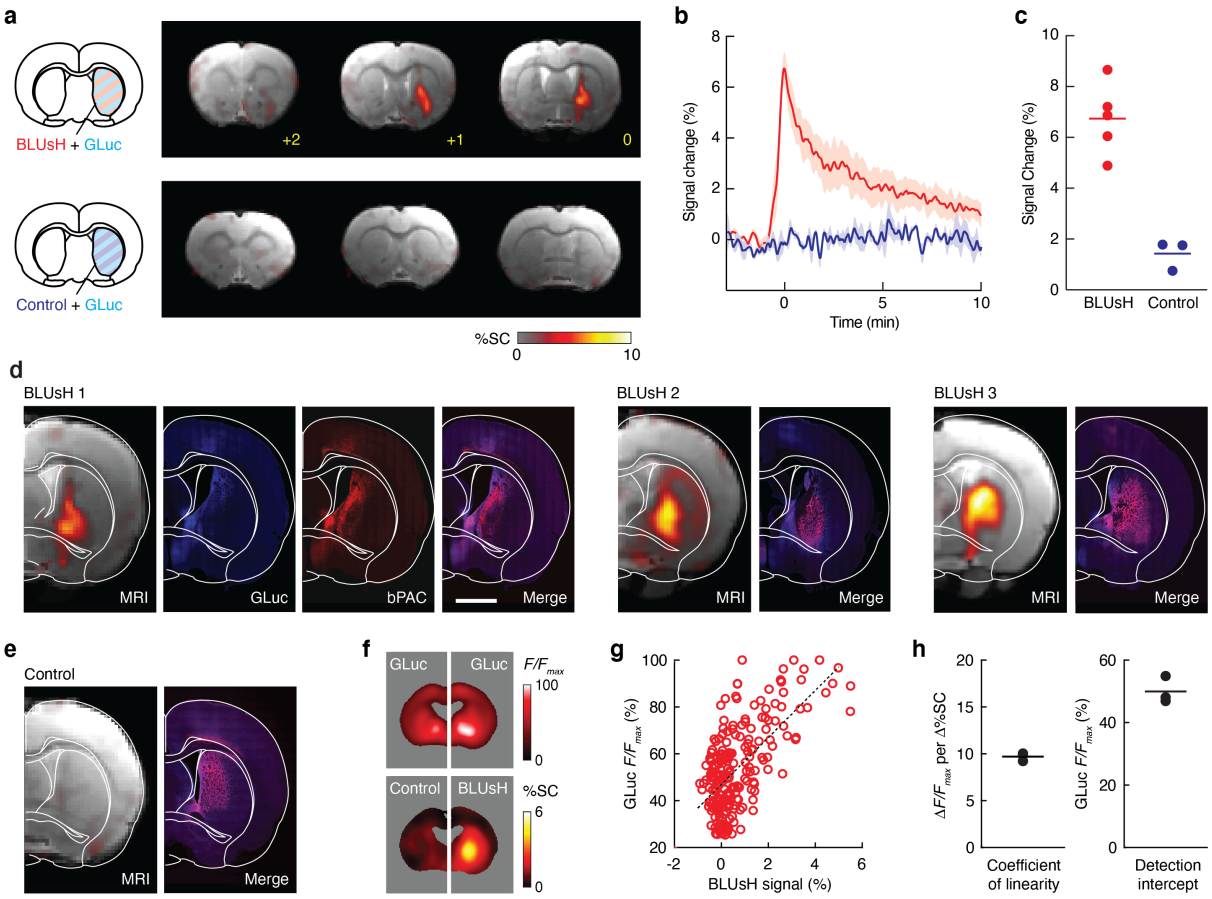

Fig. 4 | BLUsH imaging of endogenous luciferase expression. (a) BLUsH (top) or control (bottom) imaging of brain regions from representative animals transduced with viruses as schematized at left and treated intravenously with CTZ to elicit responses. Bregma coordinates in yellow. **(b)** Time courses of BLUsH and control MRI signal aligned to peak response times (time = 0 min). Shading indicates SEM of five (BLUsH) or three (control) experiments. **(c)** Peak signal change maxima observed in BLUsH and control experiments. Lines indicate average peak signal changes and dots values of single biological replicates for each group. **(d)** Comparison of signal change profiles detected by MRI-based BLUsH *vs.* postmortem histology of GLuc and bPAC expression in individual animals, showing correspondence of profiles at an individual animal level. Scale bar = 2 mm. **(e)** Null signal changes observed in a control virus-treated animal (left), compared with histology of GLuc and bPAC (right) in the same animal. **(f)** Spatial alignment of coregistered GLuc histology (top) and MRI (bottom) images indicating overlap of signals in BLUsH (right) but not control (left) brain regions. **(g)** Correspondence of GLuc histology and BLUsH signal changes in 226 voxels (dots) across three animals, revealing a strong correlation (dashed regression line, Pearson correlation $r = 0.64$, $p < 0.001$). **(h)** Consistency of slope (left) and intercept (right) of regression lines relating BLUsH signal to histological measures of GLucM23 expression in three animals.